Available online at www.sciencedirect.com
ScienceDirect
Comput. Methods Appl. Mech. Engrg. 373 (2021) 113550
Computer methods in applied mechanics and engineering
www.elsevier.com/locate/cma

Isogeometric analysis of subcutaneous injection of monoclonal antibodies

Mario de Lucio, Miguel Bures, Arezoo M. Ardekani, Pavlos P. Vlachos, Hector Gomez*

School of Mechanical Engineering, Purdue University, 585 Purdue Mall, West Lafayette, IN 47907, USA

Received 12 August 2020; received in revised form 27 October 2020; accepted 27 October 2020
Available online xxxx

Abstract

Subcutaneous injection for self-administration of biotherapeutics, such as monoclonal antibodies, has emerged as a fast-growing field in the pharmaceutical industry. Effective drug delivery in the subcutaneous tissue critically depends on the coupled mechanical and transport processes occurring in the tissue during and after the injection. The details of these processes, however, remain poorly understood; and this explains the growing interest in computational approaches. Notably, there are very few computational studies on subcutaneous injection into three-dimensional porous media that account for tissue deformability. Here, we leverage a poroelastic model to analyze the response of subcutaneous tissue under the flow of a pressurized fluid. We propose a computational method based on Isogeometric Analysis that exploits the global continuity of splines. Our model shows the importance of considering tissue deformation and permeability changes in order to obtain more realistic results in terms of fluid pressure and velocity, during and after the injection.

Keywords: Subcutaneous injection; Poroelasticity; Isogeometric analysis

1. Introduction

Biologics are becoming one of the most critical areas in the pharmaceutical industry. From rheumatoid arthritis to diabetes and cancers, these biotherapeutics have improved treatments of many diseases. Monoclonal Antibodies (mAbs) are the fastest-growing category of protein-based drugs [1]. mAbs are antibodies synthesized from cloned immune cells. mAbs are large molecules (150 kDa) that require parenteral administration, that is, delivery from routes outside of the digestive system. mAbs are usually administered through intravenous or subcutaneous routes. Subcutaneous administration is attracting great interest because it is facilitating self-administration. Subcutaneous delivery reduces the total cost of treatment, the risk of systemic infection, and is generally preferred by patients and caregivers [2–4]. An essential disadvantage of subcutaneous administration with respect to intravenous infusion is that it results in lower bioavailability.[1] The most commonly used mAbs show a bioavailability of ∼60%–80% when injected subcutaneously, which imposes a significant economic penalty given the high cost of these therapeutic compounds. The low bioavailability of mAbs can be explained by the complex transport process that they undergo.

* Corresponding author.
E-mail address: hectorgomez@purdue.edu (H. Gomez).

[1] Bioavailability is the fraction of the administered drug that reaches the systemic circulation.

https://doi.org/10.1016/j.cma.2020.113550

mAbs are too large for direct capillary uptake. They leave the injection site via the lymphatic system, and travel through it until reaching the systemic circulation. mAbs can be degraded at the injection site, or any point through the lymphatic system, including lymph nodes. The inhibitive mechanisms for mAbs transport remain unknown, but the current hypothesis suggests that interstitial transport may be the initial critical step in the process. Interstitial transport may also limit injectable drug volumes to ∼2 mL [5,6]. The volume limitation is a significant barrier and has slowed down, for example, the advance of subcutaneous administration of mAbs in cancer therapy [7,8]. One solution to the volume limitation is to make highly concentrated protein solutions, but that increases the drug's viscosity [9]. An increase in the drug's viscosity further limits transport in the interstitium and increases the stress levels undergone by the drug, augmenting the risk of protein unfolding or denaturation. Higher viscosity also creates challenges with the delivery. Forward processing of drug substance into drug product can also be challenging for high viscosity.

Our lack of understanding of the governing mechanisms limiting interstitial transport has triggered a growing interest in computational research on subcutaneous injection biomechanics [10,11]. With the notable exception of some semi-analytical axisymmetric solutions [12,13] and simplified one-dimensional models [11], the existing literature has focused on spherically-symmetric flow on a rigid porous medium [10]. Also, previous work on subcutaneous injection modeling has considered linear models with constant properties. Here, we leverage three-dimensional poroelastic models to study the tissue deformation and pressure buildup after subcutaneous injection, which are critical to reduction in injection site reactions such as edema. The pressure in the interstitium is also a critical regulator of the drug uptake. We use a linear model based on Biot's poroelasticity and a nonlinear model that accounts for changes in the permeability produced by tissue deformation. Our computational methodology is based on high-order isogeometric analysis, which has been shown to improve the stability of equal-order formulations simultaneously permitting larger time steps [14]. Isogeometric Analysis has also shown promise for poroelasticity in collocation formulations [15].

We use our simulations to assess the influence of tissue deformation on the overall poroelastic response. We compare the dynamics of subcutaneous injection on a rigid porous medium and a poroelastic medium with constant permeability, to understand how the deformable solid skeleton affects the fluid pressure and velocity. This analysis is performed for different injection depths, permeability, and stiffness properties. We also compare results for constant permeability with results for deformation-dependent permeability. We show that tissue deformation and permeability changes play a critical role in the fluid pressure distribution, velocity, and therefore, in the way the drug is delivered. Potential extensions of this research may include coupling our computational model with Physiologically Based Pharmacokinetic (PBPK) models [16] or with models of microvascular flow and lymphatic drainage [17,18].

2. Poroelastic model

Our model problem to study pressure buildup during subcutaneous injection is conceptually described in Fig. 1. We consider a piece of tissue (Fig. 1A) that goes from the skin surface to the muscle with the subcutaneous space in between. The subcutaneous tissue is the innermost layer of skin. It is primarily composed of large cells (adipocytes) that are kept in place by a fibrous network of septae primarily made of collagen. This network is continuous from the subcutaneous space to the dermis. The subcutaneous tissue hosts nerves as well as blood and lymphatic vessels. Fig. 1B shows a histological section of porcine tissue. The staining clearly shows the different layers of the tissue. Although intramuscular injections are also often used (e.g., inactivated vaccines containing an adjuvant), we will focus on subcutaneous injection, which is the most common administration method for mAbs.

2.1. Governing equations

The transport and mechanical processes occurring during subcutaneous injection are very complex and involve at least multiphase and multicomponent flows in a deformable and heterogeneous porous medium. The drug is usually a highly viscous solution, but the syringe also contains a non-negligible (up to ∼10% of the volume) amount of air. We do not model how the needle penetrates the skin [19], but only how the drug that enters the tissue during the injection produces interstitial flow and tissue deformation. Our primary interest here is to understand how the tissue deformation modifies the pressure buildup produced by the injection. To study this problem in isolation, we will focus on single-phase flow. We will also assume uniform mechanical properties of the tissue across the different

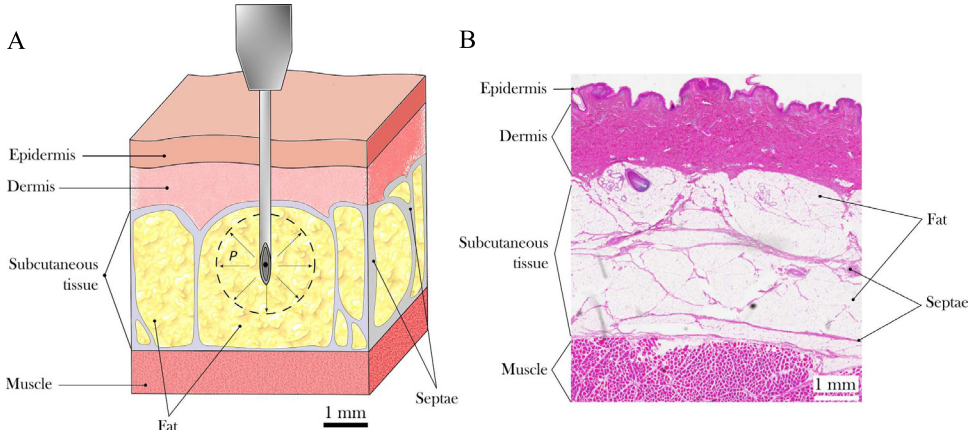

Fig. 1. (A) Schematic representation of an injection in the subcutaneous space. The simplified anatomic illustration shows the different layers of the tissue, including the epidermis, dermis, subcutaneous tissue, and muscle. (B) Histological section of porcine tissue showing the different layers through staining.

layers, but we will account for the constraining effect of the muscle layer using adequate boundary conditions. Our model is based on Biot's poroelasticity [20,21], which is governed by the equations

$$\alpha \frac{\partial \epsilon_v}{\partial t} + \frac{1}{M}\frac{\partial p}{\partial t} = \nabla \cdot \left(\frac{\kappa(\phi)}{\eta} \nabla p \right) + q \tag{1}$$

$$\nabla \cdot \boldsymbol{\sigma} = \alpha \nabla p \tag{2}$$

where α is the Biot coefficient, t is time, M is the Biot modulus, p is the pore pressure, κ is the permeability of the porous medium, which is assumed to be a function of the porosity ϕ, η is the fluid dynamic viscosity, q is a source term proportional to the mass added by the injection, and $\boldsymbol{\sigma}$ is the effective stress tensor. We will assume that the porous medium is a linear elastic material, undergoing small deformations. Thus, the effective stress tensor, $\boldsymbol{\sigma}$, is a linear function of the infinitesimal strains given by $\boldsymbol{\sigma} = \lambda \, \mathrm{tr}(\boldsymbol{\epsilon}) \boldsymbol{I} + 2\mu \boldsymbol{\epsilon}$ where λ and μ are the Lame constants, $\boldsymbol{\epsilon}$ is the infinitesimal strain tensor, $\boldsymbol{\epsilon} = \frac{1}{2}(\nabla \boldsymbol{u} + \nabla^T \boldsymbol{u})$, and $\boldsymbol{u}$ is the displacement field. In Eq. (1), $\epsilon_v = \mathrm{tr}(\boldsymbol{\epsilon})$ is the volumetric strain.

2.2. Dependence of the permeability on porosity

The rearrangement of the solid skeleton and the fluid phase produced by deformation leads to porosity changes. Even small porosity changes can significantly modify the permeability of the tissue [22]. There has been debate on how porosity changes with deformation [23], but when the deformation occurs with small volume changes in the solid particles (e.g., $\alpha \approx 1$, which is a good approximation for subcutaneous tissue), then

$$(1 - \phi) J = 1 - \phi_0 \tag{3}$$

where $J = \det(\boldsymbol{I} + \nabla \boldsymbol{u})$ is the Jacobian of the motion, and ϕ_0 is the initial porosity; see [24]. Therefore, the porosity can be expressed in terms of the deformation gradient as

$$\phi = 1 - \frac{1 - \phi_0}{\det(\boldsymbol{I} + \nabla \boldsymbol{u})} \tag{4}$$

We adopt the Kozeny–Carman equation to account for the local permeability changes,

$$\kappa(\phi) = \kappa_0 \frac{(1 - \phi_0)^2}{\phi_0^3} \frac{\phi^3}{(1 - \phi)^2} \tag{5}$$

where $\kappa_0 = \kappa(\phi_0)$ is the permeability of the undeformed porous medium. We chose the Kozeny–Carman equation because it is suitable for a wide range of materials [25,26] and it does not depend on physical properties that would be difficult to quantify in a macroscopic model of biological tissue, like the pore or grain size.

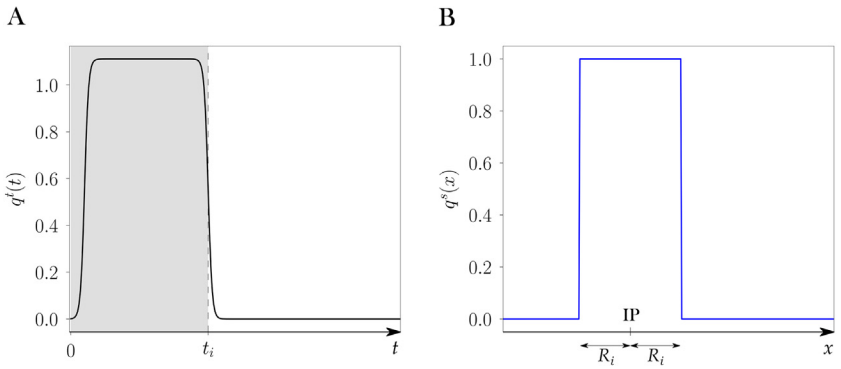

Fig. 2. Functions q^t (A) and q^s (B) used to define the source term that models the injection. In panel A the gray shadow area denotes the injection time interval, where t_i is the time at which the injection ends. In panel B, IP represents the location of the injection point and R_i is the needle radius. For simplicity we plotted the function in 1D.

2.3. Injection characterization

We assume that the injection starts at $t = 0$. We model the injection using a time and space dependent function $q(\boldsymbol{x}, t)$ that we express as $q(\boldsymbol{x}, t) = q_0 q_D^s(\boldsymbol{x}) q_D^t(t)$. Here, $q_D^t(t) = \mathcal{H}(t_i - t)$ where $\mathcal{H}$ is the Heaviside function and t_i the time at which the injection ends. We take $q_D^s(\boldsymbol{x}) = \mathcal{H}(R_i - d(\boldsymbol{x}))$ where $d(\boldsymbol{x})$ is the distance from $\boldsymbol{x}$ to the injection point and R_i is the needle radius. The scalar parameter q_0 is determined using the condition

$$\int_0^\infty \int_\Omega q(\boldsymbol{x}, t) \mathrm{d}\Omega \mathrm{d}t = V_i \tag{6}$$

where Ω represents a sufficiently large portion of tissue containing the injection point, and V_i is the volume of drug injected. Eq. (6), which leads to

$$q_0 = \frac{V_i}{t_i} \frac{1}{\frac{4}{3}\pi R_i^3} \tag{7}$$

ensures that the mass of fluid added to the tissue during injection equals the mass of drug in the injection under the assumption that drug and interstitial fluid have the same density.

To accelerate the convergence of our Newton–Raphson iterative algorithm (see Section 3), we replaced the discontinuous functions q_D^s and q_D^t by smooth approximations based on hyperbolic tangent functions such that Eq. (6) remains accurately satisfied. In particular, we used

$$q^t(t) = \frac{1}{2}\alpha_T \left[\tanh(\beta(t - t_{sh})) - \tanh(\beta(t - t_i))\right] \tag{8}$$

$$q^s(\boldsymbol{x}) = \frac{1}{2}\left[1 - \tanh\left(\Lambda(d(\boldsymbol{x}) - R_i)\right)\right] \tag{9}$$

where $\alpha_T = 10/9$, $\beta = 7\ \mathrm{s}^{-1}$, $t_{sh} = 0.5$ s, $\Lambda = 5000\ \mathrm{mm}^{-1}$. Note that $q^t(0) = 0$, but the function grows quickly to reach a plateau and then gradually drops to zero at $t = t_i$. The functions q^t and q^s are depicted in Fig. 2. The injection can also be modeled by modifying the geometry of the computational domain to account for the presence of the needle and using suitable boundary conditions. We found that our approach based on a source term in Eq. (1) is simpler and produces very similar results.

2.4. Model parameters

The characterization of the poromechanical properties of subcutaneous tissue is still in early development. A review of the existing literature reveals a significant variability in some of the poromechanical properties. To manage the uncertainty on the parameters, we performed simulations over a range of values for the tissue's properties with the most significant variability.

Table 1
Values of the model parameters.

	Description	Reference value (range)	Source
M	Bulk modulus of fluid–solid mixture	0.034 MPa (0.03–0.12)	[11]
α	Biot coefficient	1 (0.95–1)	[40,41]
η	Fluid viscosity	10^{-3} Pa s	Water viscosity
K	Hydraulic conductivity	100 mm^2/(MPa s) (50–1000)	[11,28–30]
κ_0	Permeability of the undeformed medium	10^{-13} m^2 (10^{-15}–10^{-13})	[11]
ϕ_0	Porosity of the undeformed medium	0.01 (0.01–0.05)	[11]
E	Young's modulus of the tissue	10 kPa (10–80)	[33–36]
ν	Poisson's ratio	0.45 (0.42–0.49)	[37,38]

One of the critical parameters for the fluid flow is the hydraulic conductivity of the undeformed porous medium, i.e., $K = \kappa_0/\eta$. While most previous work has assumed that the viscosity of the interstitial fluid η can be approximated by the viscosity of water, there are numerous studies reporting values of κ_0 for biological tissue; ranging from 10^{-17} m^2 for vascularized tumors [27,28], to 10^{-11} m^2 for subcutaneous tissue [11]. Intermediate values were reported in [29] (10^{-13} m^2) also for the subcutaneous space, and in [30] (10^{-12} m^2) for brain tissue. The low values of the permeability for subcutaneous tissue make the computations more challenging. To analyze the influence of the permeability on the poroelastic response, we will consider three different values: $\kappa_0 = 5 \times 10^{-14}$, 10^{-13}, and 10^{-12} m^2. For a fluid with the same viscosity as water, this leads to $K = 50$, 100, and 1000 mm^2 MPa^{-1} s^{-1}.

The mechanical properties of biological tissues vary significantly depending on the physiological conditions of the individual. We also observed variability on measurements of the tissue Young's modulus (E) depending on the experimental method. The Young's modulus of biological tissue is usually determined by indentation or tensile test. In general, the estimates based on indentation measurements are much smaller than those based on tensile tests. An excellent example of this discrepancy can be found in [31] — for human skin, 0.085 MPa using indentation and 30 MPa using tensile test; and for soft muscle, 0.007 MPa by indentation and 480 MPa utilizing tensile test. Subcutaneous tissue is softer than muscle and skin. Measurements of the Young's modulus of fat tissue also show significant variability, ranging from 0.12 to 80 kPa [32–36]. Due to the uncertainty on the Young's modulus we performed our simulations using three different values, namely, $E = 10$, 35, and 80 kPa. To select these representative values we relied more heavily on indentation measurements at the forearm because they seem more repeatable. Experimental measurements of the tissue Poisson's ratio (ν) show less variability [32,37,38]. The values used in the literature are usually in the range of $0.42 < \nu < 0.49$, which is consistent with the quasi-incompressible response of biological tissue.

The constants α and M characterize the coupled behavior of the solid and fluid constituents. The admissible values for α range from ϕ to 1; see [39]. For rock-like materials $\alpha \approx \phi$, while for biological tissues $\alpha \approx 1$ [40,41]. The Biot modulus of human subcutaneous tissue has been recently measured experimentally with values in the range 30–120 kPa [11]. Table 1 summarizes the reference values and ranges of all the model parameters. Unless otherwise specified, we will use the reference values in the simulations.

The injection is characterized by its volume V_i, delivery time t_i, and the needle radius R_i. Unless otherwise stated, we will use $R_i = 0.1$ mm, $V_i = 2$ mL, and $t_i = 5$ s, which is representative of a high flow-rate subcutaneous injection of mAbs [7,42,43]. The very high flow rates and very large injection volumes that we study here are unique to subcutaneous injection of mAbs and give rise to significant computational challenges, including strong coupling between flow and mechanics, large fluid velocities and potentially large solid deformations.

3. Numerical method

The spatial discretization of the governing equations is performed using isogeometric analysis (IGA) [44]. IGA is a generalization of the finite-element method that uses non-uniform rational B-splines (NURBS) to define the discrete spaces. A significant advantage of IGA with respect to finite element analysis is that the basis functions can be constructed with controllable continuity across the element boundaries, even on mapped geometries. The higher-order global continuity of the basis functions has been shown to produce higher accuracy than classical C^0-continuous finite elements for the same number of degrees of freedom [45,46]; and has been widely used to solve

partial differential equations with high-order spatial derivatives [47–49]. Another advantage of using basis functions with global continuity is the possibility of using geometrically flexible collocation methods [50] which can be made as accurate as the Galerkin method with a proper choice of the collocation points [51]. Higher-order global continuity has also proven effective in alleviating locking problems in incompressible elasticity [52–54] or *inf–sup* instabilities in linear poroelasticity [14,15]. As shown in [55], for some parameter ranges, displacement–pressure ($\boldsymbol{u} - p$) finite element formulations of the poroelasticity equations need to satisfy Ladyzhenskaya–Babuška–Brezzi (LBB) conditions similar to those required for $\boldsymbol{u} - p$ formulations of incompressible elasticity. For the LBB conditions to be satisfied, the pressure field p needs to be approximated with a lower-dimensional discrete space than the displacement field $\boldsymbol{u}$, although formulations that violate the LBB conditions are standard [56–58]. In particular, equal-order interpolations using higher-order splines of maximum continuity have proven very effective [14]. Here, we will use $\mathcal{C}^2$-continuous cubic splines for $\boldsymbol{u}$ and p. Consistently with [14], we found that, although the algorithm does not provide a fundamental solution to the *inf–sup* stability problem, it provides oscillation-free solutions in a large parametric range.

3.1. Weak form

The strong form of our hydraulic–mechanical coupled model defined by Eqs. (1), (2), (4) and (5) is now cast in weak form and discretized using the Galerkin approach. For the pressure field, we will work with either free-flux or zero-valued Dirichlet boundary conditions. For the displacement field, we assume either zero-valued Dirichlet boundary conditions or traction-free conditions. With these boundary conditions, all boundary integrals will vanish in the weak form. Let us define the functional space $\mathcal{V} \subset \mathcal{H}^1$, where $\mathcal{H}^1$ is the Sobolev space of square-integrable functions with square-integrable first derivatives in the domain Ω. To perform space discretization we introduce the finite-dimensional space $\mathcal{V}^h \subset \mathcal{V}$, where $\mathcal{V}^h = \text{span}\{N_A\}_{A=1,\dots,n_f}$ and n_f is the number of functions on the basis. The space of weighting functions will also be $\mathcal{V}^h$, giving rise to a Galerkin formulation. We define discrete approximations to the problem's solution denoted by p^h and $\boldsymbol{u}^h = \left\{u_i^h\right\}_{i=1,2,3}$. Their corresponding weighting functions are r^h and $\boldsymbol{w}^h = \left\{w_i^h\right\}_{i=1,2,3}$. Then, the variational formulation of Eqs. (1)–(2) over the finite-dimensional space $\mathcal{V}^h$ can be stated as follows: find $p^h, u_i^h \in \mathcal{V}^h \subset \mathcal{V}$ such that $\forall r^h, w_i^h \in \mathcal{V}^h \subset \mathcal{V}$

$$\int_\Omega r^h \frac{1}{M}\frac{\partial p^h}{\partial t}\mathrm{d}\Omega + \int_\Omega \alpha r^h \frac{\partial\left(\nabla\cdot\boldsymbol{u}^h\right)}{\partial t}\mathrm{d}\Omega + \int_\Omega \frac{\kappa\left(\phi(\boldsymbol{u}^h)\right)}{\eta}\nabla r^h\cdot\nabla p^h\mathrm{d}\Omega - \int_\Omega r^h q\mathrm{d}\Omega = 0 \tag{10}$$

$$\int_\Omega 2\mu\nabla^S\boldsymbol{w}^h : \nabla^S\boldsymbol{u}^h\mathrm{d}\Omega + \int_\Omega \lambda\nabla\cdot\boldsymbol{w}^h\nabla\cdot\boldsymbol{u}^h\mathrm{d}\Omega - \int_\Omega \alpha\nabla\cdot\boldsymbol{w}^h p^h\mathrm{d}\Omega = 0 \tag{11}$$

where ∇^S denotes the symmetrization of the gradient operator. The solutions p^h and $\boldsymbol{u}^h$ are defined as

$$p^h(\boldsymbol{x},t) = \sum_{A=1}^{n_f} p_A(t)\,N_A(\boldsymbol{x})\,; \quad \boldsymbol{u}^h(\boldsymbol{x},t) = \sum_{A=1}^{n_f}\boldsymbol{u}_A(t)\,N_A(\boldsymbol{x}) \tag{12}$$

where the coefficients p_A and $\boldsymbol{u}_A$ are the so-called control variables in the context of IGA. The weight functions r^h and $\boldsymbol{w}^h$ are defined analogously.

3.2. Time integration

A somewhat counterintuitive feature of the poroelasticity equations is that they exhibit oscillatory numerical solutions when the time step is *smaller* than a critical value. Ref. [59] shows that the stability condition for a 1D problem using linear finite elements and the generalized trapezoidal method [60] is

$$\Delta t \geq \frac{h^2}{6\theta\alpha K M} \tag{13}$$

where h is the mesh size and $\theta \in (0, 1]$ is a parameter of the generalized trapezoidal method. For $\theta = 0$, 1/2 and 1, the generalized trapezoidal rule becomes, respectively, the forward Euler method, the midpoint rule and the backward Euler method. Although the stability condition given by Eq. (13) was derived under restrictive assumptions it has been widely used in multidimensional problems with higher-order elements. Recent work [14,61] shows that

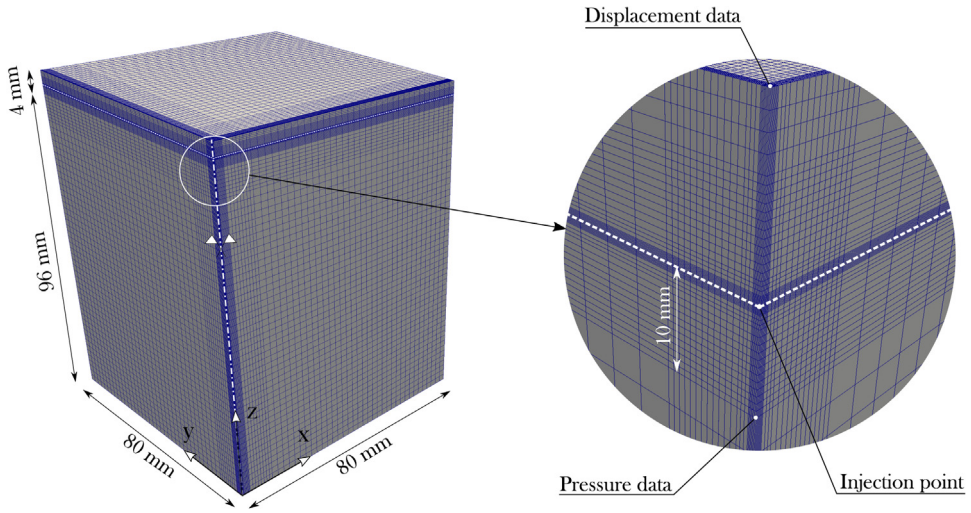

Fig. 3. Computational domain, mesh and points at which we report data. The mesh is refined in the vicinity of the injection point to resolve the large pressure gradients produced by the injection.

if (13) is violated, the use of maximum-continuity isogeometric elements significantly reduces the oscillations for classical C^0-continuous finite elements.

We performed time integration using the generalized-α method [62,63]. As shown in [62], this algorithm allows to control high-frequency dissipation maintaining second-order accuracy and A-stability. The high frequency dissipation is controlled using the parameter ρ_∞, which represents the spectral radius of the amplification matrix as $\Delta t \to \infty$. In our calculations, we took $\rho_\infty = 1/2$. The generalized-α algorithm does not belong to the generalized trapezoidal family of methods, but we assumed that $\theta = 2/3$ is an acceptable value to estimate the critical time step. Because of the additional stability provided by the use of isogeometric elements, we expect that Eq. (13) represents a conservative estimate of the critical time step. This expectation was consistent with our oscillation-free results.

The system of algebraic equations that we obtain after space and time discretization is nonlinear due to the dependence of the permeability on the displacement field; see Eqs. (4)–(5). We linearized the algebraic equations using the Newton–Raphson method. To linearize $\kappa\left(\phi(\boldsymbol{u}^h)\right)$ we used a consistent linearization that follows from Eqs. (4)–(5) and the chain rule. We solved the problem monolithically. For an in-depth comparison of monolithic and staggered schemes, see [64]. For most simulations in the paper, the problem is linear and the Newton–Raphson algorithm converges in one iteration if the tolerance of the linear solver is set sufficiently low. When the permeability depends on porosity the problem becomes nonlinear and we need to perform multiple Newton–Raphson iterations. Most of the time steps required 4 iterations. The resulting linear systems were solved using the GMRES algorithm with a diagonal preconditioner [65].

4. Numerical results

We study the injection process on a tissue of size 160 mm $\times$ 160 mm $\times$ 100 mm. Using the symmetry of the solution, we perform computations on the box $\Omega = (0, 80) \times (0, 80) \times (0, 100)$, where the units are in mm; see Fig. 3. The planes $x = 0$ and $y = 0$ are symmetry planes and we use standard symmetry boundary conditions for the displacement field and the pressure. On the other two vertical planes ($x = 80$ mm and $y = 80$ mm), we impose traction-free boundary conditions for the displacement field. For the pressure boundary conditions on the $x = 80$ mm and $y = 80$ mm planes, we study two scenarios: (1) Undrained, i.e., flux-free boundary conditions, and (2) Drained, i.e., zero-pressure boundary conditions. On the top boundary, which represents the skin, we impose traction-free and flux-free boundary conditions. On the bottom boundary, we use zero-displacements and flux-free boundary conditions for the pressure. The injection point is located 4 mm below the skin surface, at the point (0,0,96) mm. An injection depth of 4 mm would typically place the needle tip in the subcutaneous space for an average human tissue sample from the thigh or the abdomen. However, due to the significant variability in the

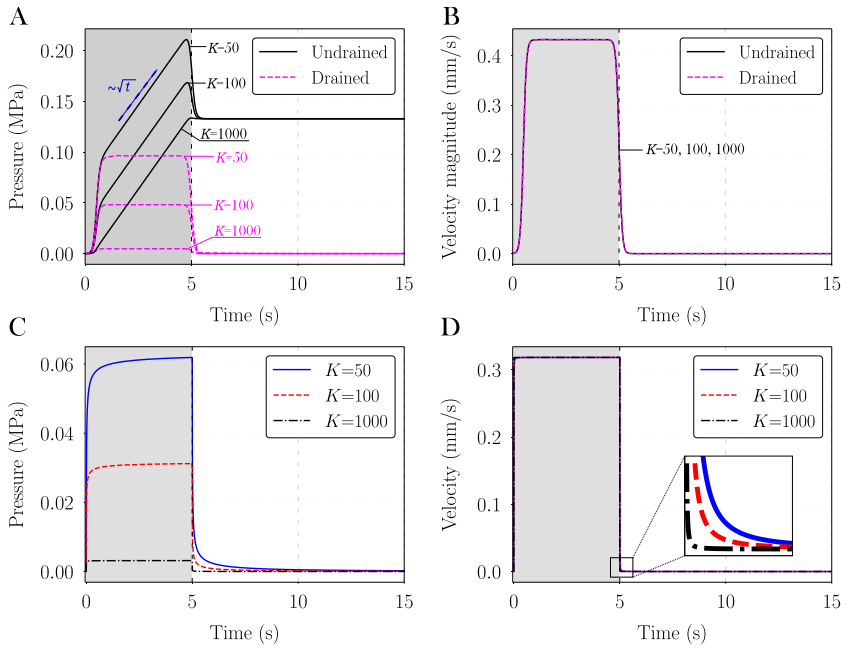

Fig. 4. Numerical solution for the fluid pressure (A) and velocity (B) over time at a point located 10 mm below the injection point for different hydraulic conductivity K (mm^2 MPa^{-1} s^{-1}) values, and different boundary conditions. Exact solution to Eqs. (15)–(16) in 3D [see Eq. (20)] for the fluid pressure (C) and velocity (D) over time at a point 10 mm away from the injection point, also for different values of K. The gray shadow area denotes the injection time interval in all plots.

thickness of the tissue layers, we also performed simulations with injections at a 10 mm depth. These calculations (data not shown) were qualitatively similar to the results presented in the paper.

Unless otherwise specified, for all the simulations shown in the paper we used the mesh depicted in Fig. 3. The mesh is finest at the injection point. The total number of elements is 453,024. We used $\mathcal{C}^2$-continuous cubic basis functions for the displacements and pressure. Our code was developed using PetIGA [66], a library that adds spline and integration of forms capabilities to the linear algebra package PETSc [67].

4.1. Injection on a rigid porous medium

To establish a reference point and evaluate the impact of tissue deformation on the dynamics of pressure buildup during the injection, we present here numerical simulations on a rigid porous medium, which have been often used in the literature to study subcutaneous injection [10]. To better understand the effect of boundary conditions and our strategy to model the injection (see Section 2.3), we also compare our simulations on rigid porous media with exact solutions on an infinite three-dimensional domain in which the injection is modeled using a Dirac delta distribution. For a rigid porous medium, the governing equations are

$$\frac{1}{M}\frac{\partial p}{\partial t} = \nabla \cdot (K \nabla p) + q \tag{14}$$

where $M = \phi / K_f$. Here, K_f, the bulk modulus of the fluid was estimated as follows: Drugs based on mAbs are frequently injected in the subcutaneous tissue using an autoinjector. The syringe of the autoinjector contains a liquid solution with the drug (∼90% of the volume) and air (∼10% of the injection volume). There is no data on how air affects the bulk modulus of the drug solution, but there is abundant experimental data showing that even small air volume fractions can reduce the bulk modulus of air–water mixtures well below that of air itself [68–70]. In the absence of better data, we estimated K_f using the experimental data for an air–water mixture with a 10% volume fraction of air, which results in $K_f \approx 1.7$ MPa. For the computational results, q is defined as described in Section 2.3. Fig. 4A shows the time evolution of the fluid pressure at a point located 10 mm below the injection

point (see Fig. 3) using our numerical algorithm. The plot shows the solution for the two boundary conditions studied (drained and undrained) and illustrates that the pressure dynamics strongly depends on boundary conditions for a rigid porous medium. Under drained conditions, the pressure quickly develops a plateau and drops to zero immediately after the injection ends. Assuming undrained boundary conditions, the pressure grows closely matching a $\sim t^{1/2}$ scaling and then drops to a level that depends on the injection volume and the domain size. The data also show that, for a given time, the pressure grows when the permeability decreases as expected. Fig. 4B shows the time evolution of the fluid velocity at the same point, which is insensitive to the boundary conditions and the permeability.

We now compare the numerical solutions using the approach described in Section 2.3 to model the injection (Fig. 4A and B) with the exact solution to the problem utilizing a Dirac delta distribution, that is,

$$\frac{1}{M}\frac{\partial p^e_{d_s}}{\partial t} = \nabla\cdot(K\nabla p^e_{d_s}) + q^e_{d_s}\delta_{d_s}(\boldsymbol{x}-\boldsymbol{x}_i)\mathcal{H}(t_i-t);\ \ \boldsymbol{x}\in\mathbb{R}^{d_s},\ \ t>0 \tag{15}$$

$$p^e_{d_s}(\boldsymbol{x},0) = 0;\ \ \boldsymbol{x}\in\mathbb{R}^{d_s} \tag{16}$$

In Eq. (15), δ_{d_s} represents the Dirac delta in d_s spatial dimensions, $\boldsymbol{x}_i$ is the injection point and $q^e_{d_s}$, which has units of Length^{d_s}/Time, is a measure of the injection flow rate. In 3D ($d_s = 3$), $q^e_{d_s}$ can be directly obtained as $q^e_{d_s} = V_i/t_i$, but in lower-dimensional spaces $q^e_{d_s}$ cannot be estimated from the physical parameters that define the injection. Using Fourier transforms, we obtained the exact solution to Eqs. (15)–(16) in d_s spatial dimensions as

$$p^e_{d_s}(\boldsymbol{x},t) = q^e_{d_s}M\int_0^t \frac{\mathcal{H}(t_i-\tau)}{[4\pi KM(t-\tau)]^{d_s/2}}\exp\left(-\frac{d^2(\boldsymbol{x})}{4KM(t-\tau)}\right)\mathrm{d}\tau \tag{17}$$

where $d(\boldsymbol{x})$ is the distance from the injection point to $\boldsymbol{x}$. The expression in Eq. (17) can be written as a simple closed-form solution in a 1D ($d_s = 1$) or 3D ($d_s = 3$) space, but it is more complicated in 2D ($d_s = 2$). Interestingly, both the pressure and velocity blow up at the injection point for $d_s > 1$. For $d_s = 1$, velocity and pressure remain finite at the injection point, but the velocity is discontinuous. Because velocity and pressure blow up at the injection point for $d_s > 1$ and $q^e_{d_s}$ cannot be estimated from the physical parameters when $d_s = 1$, we conclude that the model (15)–(16) is inadequate for quantitative predictions of pressure and velocity, at least close to the injection point. In 3D, the solution (17) is spherically symmetric. Therefore, it is identical to one obtained using expressions in spherical coordinates and assuming constant solution along the angular coordinates. Note that to obtain the solution in spherical coordinates, we would need to use curvilinear coordinates not only for the differential operators but also for the Dirac delta. Therefore, the spherically symmetric solution also blows up at the injection point. The singularity at the injection point for $d_s > 1$ suggests that modeling the injection using Dirac delta distributions is inadequate and highlights the importance of our strategy for modeling the injection (see Section 2.3) in the computational approach.

In 1D, the exact solution in Eq. (17) can be expressed as

$$\begin{aligned} p^e_1(x,t) = {} & \frac{q^e_1\sqrt{M}}{\sqrt{\pi K}}\left\{\sqrt{t}\exp\left(\frac{-(x-x_i)^2}{4KMt}\right) - \sqrt{\max(0,t-t_i)}\exp\left(\frac{-(x-x_i)^2}{4KM\max(0,t-t_i)}\right)\right\} \\ & + \frac{q^e_1}{2K}\left\{(x-x_i)\,\mathrm{erf}\left(\frac{x-x_i}{2\sqrt{KMt}}\right) - (x-x_i)\,\mathrm{erf}\left(\frac{x-x_i}{2\sqrt{KM\max(0,t-t_i)}}\right)\right\} \end{aligned} \tag{18}$$

where erf denotes the error function defined as

$$\mathrm{erf}(x) = \frac{1}{\sqrt{\pi}}\int_{-x}^{+x}\exp(-s^2)\mathrm{d}s. \tag{19}$$

Eq. (18) shows that the pressure at the injection point in 1D exhibits a perfect scaling $\sim t^{1/2}$ during the injection phase ($0 < t < t_i$). That scaling law is lost as we move away from the injection point, but it remains fairly accurate ($R^2 = 0.9931$) at $x = 10$ mm (data not shown). Thus, the 1D solution and our 3D numerical solutions for undrained boundary conditions (see Fig. 4A) show a similar scaling of pressure with respect to time. This can be understood noting that the 1D solution satisfies the undrained boundary conditions in y and z directions.

In 3D, Eq. (17) can be written as

$$p^e_3(\boldsymbol{x},t) = \frac{q^e_3}{4\pi K}\frac{1}{d(\boldsymbol{x})}\left[\mathrm{erf}\left(\frac{d(\boldsymbol{x})}{2\sqrt{KM\max(t-t_i)}}\right) - \mathrm{erf}\left(\frac{d(\boldsymbol{x})}{2\sqrt{KMt}}\right)\right] \tag{20}$$

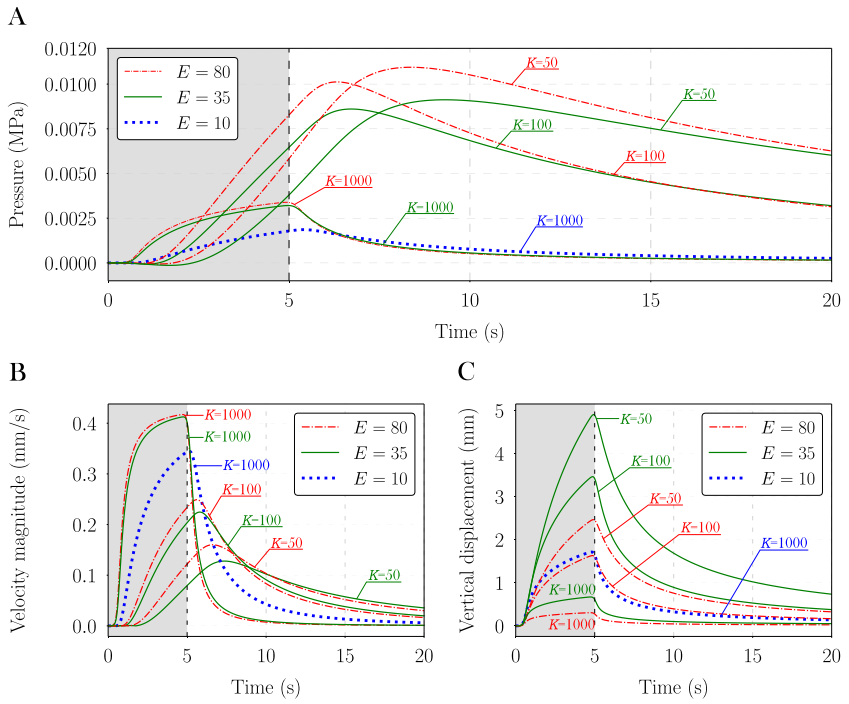

Fig. 5. Time evolution of the fluid pressure (A), velocity (B) and vertical displacement of the solid matrix (C) for the poroelastic medium with constant permeability for different values of the hydraulic conductivity K (mm^2 MPa^{-1} s^{-1}) and Young's modulus E (kPa). The gray shadow area denotes the injection time interval in all plots.

Fig. 4C shows the time evolution of the fluid pressure at a point 10 mm away from the injection point using Eq. (20). Qualitatively, the solution is similar to the numerical solution with a distributed source term and drained boundary conditions (Fig. 4A, dashed line) except at the times when the injection starts and ends. We attribute these differences to the use of q^t [see Eq. (8)] as an approximation to $\mathcal{H}(t_i - t)$. Another similitude between the pressure plots in Fig. 4C and the undrained solutions in Fig. 4A is that the maximum pressure shows a scaling $\sim K^{-1}$. Comparing again Figs. 4A and 4C we observe that the quantitative values of the pressure 10 mm below the injection are in the same order of magnitude. However, they would become very different as we approach the injection point due to the singularity of the exact solution with a Dirac delta source. The velocity predicted by the exact solution (Fig. 4D), which can be calculated by taking the spatial derivative of Eq. (20) and using Darcy's law, is also qualitatively similar with the exception that the plateau develops faster and drops more quickly after the injection ends because the source term used in the computations changes gradually rather than infinitely fast (exact solution).

4.2. Injection on a poroelastic medium

Considering the tissue deformability produces very significant changes in the time evolution of pressure and fluid velocity. One crucial difference with respect to the simulations on a rigid porous medium is that the drained and undrained boundary conditions produce indistinguishable results. Thus, we will show results for the drained boundary conditions only. In this section, we will neglect the dependence of the permeability on the porosity and use a constant value of K.

Fig. 5 shows the time evolution of the fluid pressure, fluid velocity, and vertical displacement of the solid. The pressure and velocity are measured 10 mm below the injection point, while the displacement data is taken at the skin surface on top of the injection point (see Fig. 3). The simulations are performed for $E = 10$, 35 and 80 kPa; and $K = 50$, 100 and 1000 mm^2 MPa^{-1} s^{-1}. Fig. 5A shows that the time evolution of the pressure is very different from that of a rigid porous medium. First, the maximum pressure is at least one order of magnitude lower in the

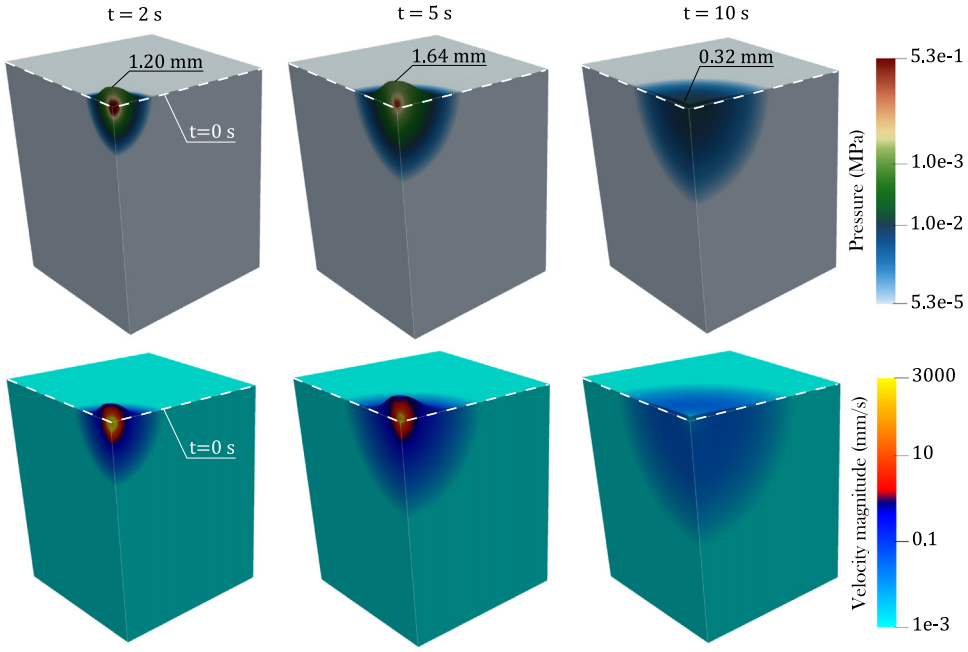

Fig. 6. Snapshots of the spatial distribution of fluid pressure and velocity for constant permeability taking $E = 10$ kPa and $K = 1000$ mm^2 MPa^{-1} s^{-1}. The rest of the parameters take the reference values. We also show the maximum vertical displacement at each time. The white dashed line depicts the position of the upper surface at $t = 0$ s. A deformation scale factor of 5 has been applied to all the figures.

poroelastic case. Second, the pressure changes in response to the injection are slower in the poroelastic medium — the pressure grows more slowly after the injection initiation and it also drops more slowly after the injection ends. For a given hydraulic conductivity, the peak pressure increases as the tissue stiffness grows. As expected, for a given Young's modulus, the peak pressure is lower and occurs earlier for larger values of the hydraulic conductivity.

Fig. 5B shows the time evolution of the fluid velocity. Using the peak values as our metric, the difference between the results of the poroelastic model and the results of the rigid model are much smaller for the velocity than they were for the pressure. An important difference between the rigid and the poroelastic models, however, is that the evolution of the velocity depends significantly on the hydraulic conductivity for the poroelastic model. For a given hydraulic conductivity the data show that the peak velocity decreases as the solid becomes softer. However, the velocity decay after the injection is slower in softer tissues.

The time evolution of displacements is shown in Fig. 5C. For a constant value of K, the peak displacements scale approximately linearly with the Young's modulus. For the largest values of the hydraulic conductivity, the displacement almost saturates to a plateau within the injection time, while for the lowest values there is significant growth of the displacement throughout the entire injection time interval.

We study the spatial distribution of pressure and velocity in Fig. 6. The colormaps are in logarithmic scales to reflect the entire range of pressure and velocity, which grow very quickly as we approach the injection point. The maximum pressure reached at the injection point is ∼0.53 MPa. This is in contrast with the unbounded value predicted by the exact solution for rigid porous media based on Dirac delta distributions and highlights the importance of modeling the injection as a distributed source and considering tissue deformation. The maximum pressure at the injection point is indeed a quantity of interest because it could control, for example, the probability of hydraulic fracture in the tissue.

The bottom row of Fig. 6 shows the velocity distribution calculated as $\boldsymbol{v} = -K\nabla p$. Because we used globally $\mathcal{C}^2$-continuous elements to approximate the pressure field, the velocity is smooth, which is an important advantage of isogeometric analysis for this problem. The maximum velocity in the simulation is 3.1004 m/s. If we divide the volume flow rate by the relevant area we obtain a theoretical velocity at the needle of 3.1831 m/s. We consider our numerical result very accurate, given that the numerical velocity was obtained from the pressure using the gradient filter in Paraview instead of taking the derivatives with the spline basis functions. The accuracy of the

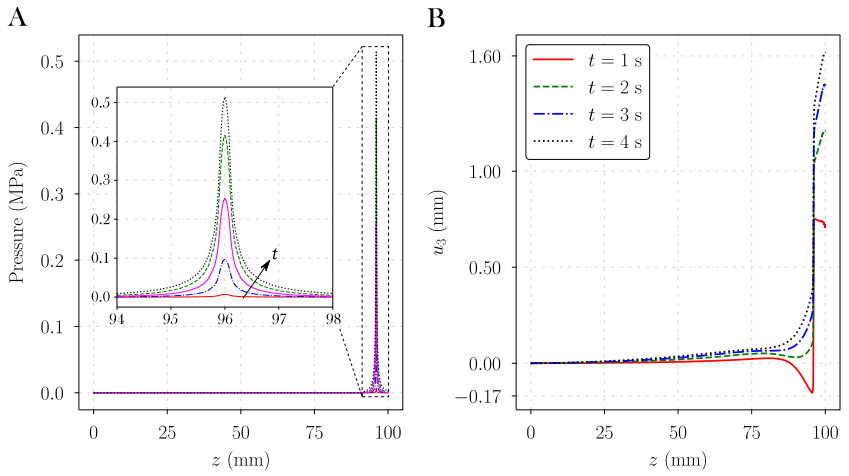

Fig. 7. Cutlines of the numerical solution for the fluid pressure (A) and vertical displacement (B) along a line parallel to the z-axis that goes through the injection point at different times for a constant hydraulic conductivity of $K = 1000$ mm^2 MPa^{-1} s^{-1}. The injection point is located at $z = 96$.

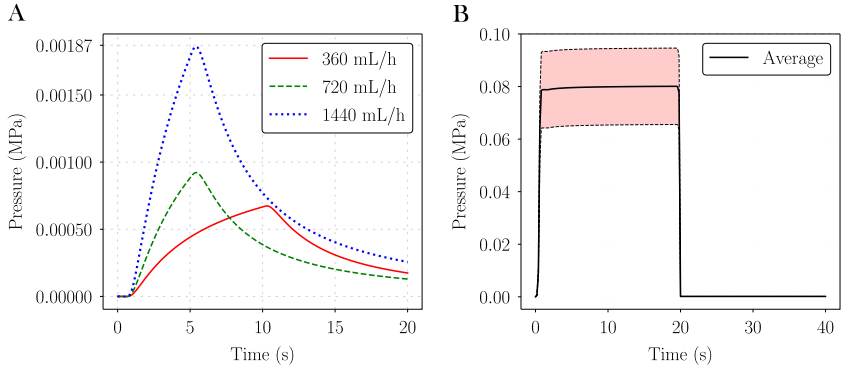

Fig. 8. (A) Effect of flow rate upon the time evolution of pressure 10 mm below the injection point. (B) Time evolution of the pressure in the spatial region occupied by the needle tip. The black line shows the spatial average and the red shade the range of pressure values in the spatial region of interest. The flow rate is 360 mL/h and the needle radius is $R_i = 0.13$ mm.

velocity becomes even more apparent by examining the large pressure gradients that occur close to the injection point. Fig. 7A shows cutlines of the pressure field at different times along a line parallel to the z-axis that goes through the injection point. The gradients are localized close to the injection point ($z = 96$) and can be more clearly observed in the inset. Fig. 7B shows that the displacements in z direction along the same cutline also exhibit very large gradients. In all cases, the numerical solution is oscillation-free highlighting the accuracy and robustness of $\mathcal{C}^2$ cubic splines.

Fig. 8 studies the effect of the volume flow rate on the pressure dynamics. Panel A shows the time evolution of the pressure 10 mm below the injection point. The variations in volume flow rate in Fig. 8A were modeled changing the injection volume and the delivery time, but the needle radius was kept constant at $R_i = 0.1$ mm. Fig. 8B shows the time evolution of the average (black line) pressure as well as its region occupied by the needle tip for a flow rate of 360 mL/h and a needle radius of $R_i = 0.13$ mm. The time evolution of pressure at the injection point is very different from that 10 mm below the injection. The peak pressure is achieved right after the injection begins. The pressure drop after the injection is also much faster at the injection point. Although we made no attempt to match the very little experimental data available in the literature (due to the uncertainty in the tissue parameters) we found that our predicted peak pressure is in reasonably good agreement with the experimental data reported in [42] for the same injection conditions (∼60 kPa).

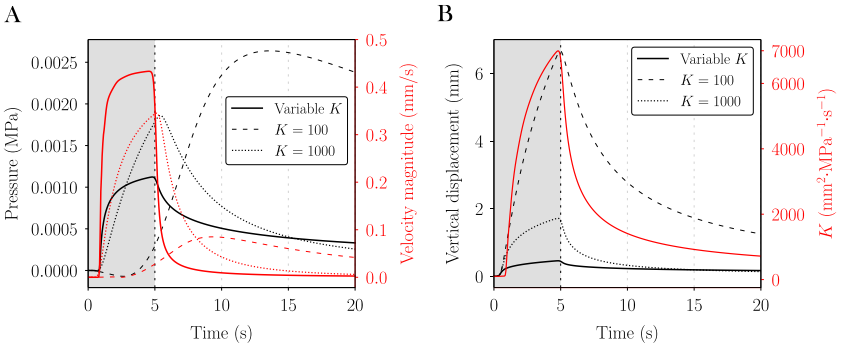

Fig. 9. Time evolution of the fluid pressure, velocity (A), solid vertical displacement and hydraulic conductivity (B) for a poroelastic medium with variable permeability (solid line), and a poroelastic medium with constant hydraulic conductivity values of $K = 100$ (dashed line) and $K = 1000$ mm^2 MPa^{-1} s^{-1} (dotted line). The time course of pressure, velocity and hydraulic conductivity are measured 10 mm below the injection point. The vertical displacements correspond to the upper surface on top of the injection point.

In summary, our simulations in poroelastic media indicate that neglecting tissue deformation leads to significant overestimations of the fluid pressure and velocity during the injection and significant underestimations of the fluid velocity after the injection ends. Although the pressure decay after the injection is slower when the tissue deformation is considered, it is still very fast compared with the time scale of drug uptake (∼5 days). Because high interstitial pressure is an important driving force for drug uptake, it is tempting to assume that the hydraulic conductivity of the tissue is lower, but this would lead to unrealistically high pressures at the injection point. Thus, we speculate that there may be additional physical mechanisms that promote a slower pressure decay while maintaining an average hydraulic conductivity that is compatible with experimental data. One such mechanism is the porosity-dependent hydraulic conductivity formulation described in Section 2.2. We study this mechanism in the next section.

4.3. Variable porosity and permeability

We perform only one simulation for $E = 10$ kPa and $\kappa_0 = 10^{-13}$ m^2. For a fluid with the same viscosity as water, this leads to an initial hydraulic conductivity of $\kappa_0/\eta = 100$ mm^2 MPa^{-1} s^{-1}. Because the simulations were exhibiting *inf–sup* instabilities near the injection point, we used a finer mesh for this case. This new mesh has a total of 1,317,260 elements, and it is also finest at the injection point.

In Fig. 9 we plot the time evolution of fluid pressure, velocity and hydraulic conductivity 10 mm below the injection point, as well as the vertical displacement of the upper surface (see Fig. 3). Fig. 9A shows that for constant permeability with $K = 100$ mm^2 MPa^{-1} s^{-1}, the pressure grows slowly after the injection and decays very slowly after the injection. In this scenario, there would be a driving force for drug uptake for a long time after the injection. However, the pressure at the injection point for constant permeability with $K = 100$ mm^2 MPa^{-1} s^{-1} is ∼5 MPa (data not shown), which seems unrealistic given the stiffness of the tissue — for comparison purposes the maximum pressure at the injection point is ∼0.5 MPa for constant permeability with $K = 1000$ mm^2 MPa^{-1} s^{-1} (see Fig. 6) and ∼0.005 MPa for non-constant permeability (see Fig. 11). As shown in Fig. 9, for the case with non-constant permeability the pressure 10 mm below the injection point at t=20 s is larger than with constant permeability and $K = 1000$ mm^2 MPa^{-1} s^{-1}, even if the peak pressure is two orders of magnitude lower for non-constant permeability. Therefore, it would be interesting to perform a computation with variable permeability and a smaller value of the initial conductivity κ_0/η. This would lead to an even slower pressure decay after the injection and a larger pressure at the injection point, closer to the realistic value ∼0.5 MPa shown in Fig. 6. However, this remains as an open problem — we have been unable to get oscillation-free solutions for such a problem due to the *inf–sup* instabilities.

Fig. 9A also shows the time evolution of fluid velocity. For a given Young's modulus of $E = 10$ kPa, the peak velocity in the medium with variable permeability is 5 times higher than that of the medium with a constant hydraulic conductivity of $K = 100$ mm^2 MPa^{-1} s^{-1}, and 1.3 times higher than that of the medium with a constant

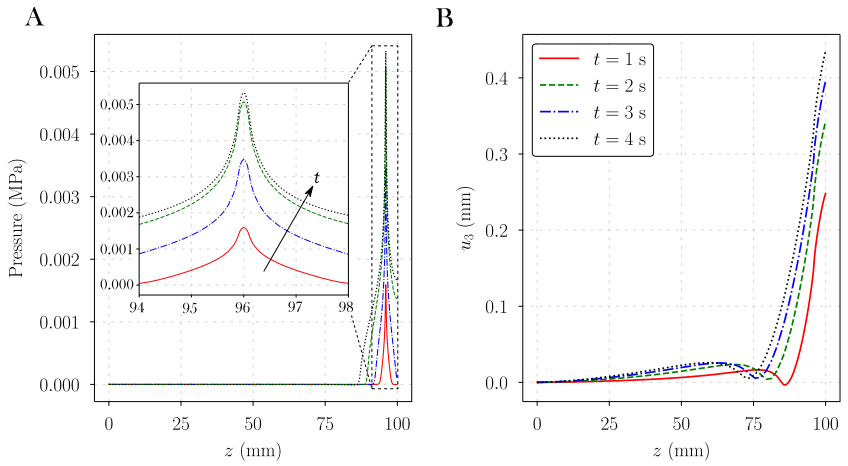

Fig. 10. Cutlines of the numerical solution for the fluid pressure (A) and vertical displacement (B) along a line parallel to the z-axis that goes through the injection point at different times for the poroelastic medium with variable permeability. The injection point is located at $z = 96$.

hydraulic conductivity of $K = 1000$ mm^2 MPa^{-1} s^{-1}. The velocity decay after the injection is stopped is also faster in the medium with variable permeability — at $t = 20$ s the velocity in the medium with variable permeability is 100 times lower than that of the medium with a constant hydraulic conductivity of $K = 100$ mm^2 MPa^{-1} s^{-1}.

Fig. 9B shows the time evolution of vertical displacements and hydraulic conductivity. The displacement data is given at the same point as before (see Fig. 3), and the hydraulic conductivity is reported 10 mm below the injection point. For a given Young's modulus of $E = 10$ kPa, the maximum displacement in the poroelastic medium with variable permeability is 15 times lower than that of the poroelastic medium with a constant hydraulic conductivity of $K = 100$ mm^2 MPa^{-1} s^{-1}. The hydraulic conductivity 10 mm below the injection point grows fast from $K = 100$ to $K = 7000$ mm^2 MPa^{-1} s^{-1} in just 5 s. After the end of the injection the decay is also fast, dropping to 700 mm^2 MPa^{-1} s^{-1} at $t = 20$ s. The large values of K in the vicinity of the injection point highlight again the interest of performing simulations with non-constant permeability and lower values of κ_0/η.

Now we focus on the cutlines of the pressure and displacement fields shown in Fig. 10. The numerical results obtained at the injection point for the poroelastic medium with variable permeability are very different from those of the poroelastic medium with constant permeability; see Fig. 7. First, the pressure decreases more slowly as we move away from the injection point in the medium with variable permeability than in the medium with constant permeability and $K = 1000$ mm^2 MPa^{-1} s^{-1}. Second, the pressure at the injection point is two orders of magnitude lower than that of the poroelastic medium with a constant hydraulic conductivity of $K = 1000$ mm^2 MPa^{-1} s^{-1}, and three orders of magnitude lower than that of the medium with a constant hydraulic conductivity of $K = 100$ mm^2 MPa^{-1} s^{-1} (data not shown). This further highlights the idea that using a low but constant permeability to slow down the pressure decay is not a feasible mechanism because it would lead to unrealistically high pressures at the injection point. Fig. 10B shows that the displacements in z direction along the same cutline also exhibit smaller gradients in the medium with variable permeability. In the medium with constant K we observe a sudden increment of the displacements at $z = 96$. In the medium with variable permeability this increment starts between $z = 74$ and $z = 85$, and it is more gradual.

Fig. 11 shows the spatial distribution of fluid pressure, velocity and porosity at different times. The changes generated by the variable permeability law lead to a different pressure decay as we move away from the injection point, and also different bleb shapes on the upper surface. The bumps on the skin surface of the simulations with variable permeability are smaller but remain longer in time. The maximum velocity in the simulation is 3.16 m/s, which is very similar to the maximum velocity values obtained for the media with constant permeability. The maximum porosity value reached at the injection point is $\sim$0.14.

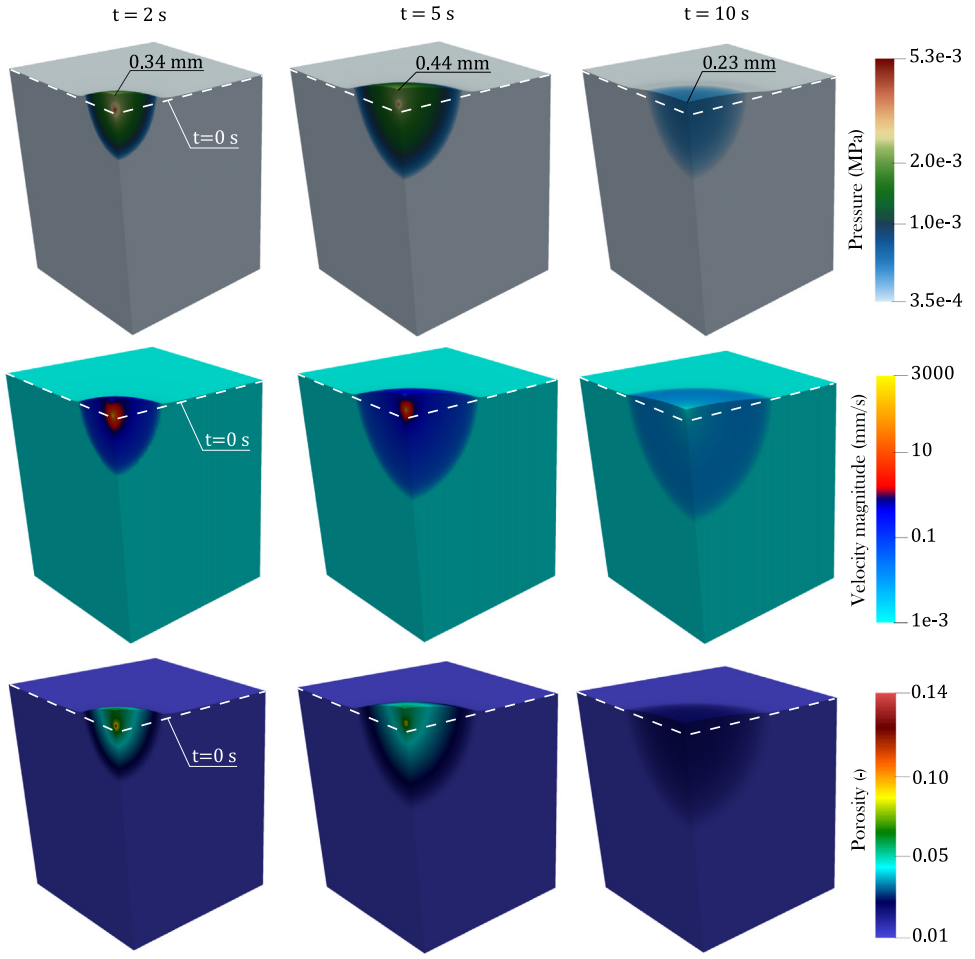

Fig. 11. Snapshots of the spatial distribution of fluid pressure, velocity and porosity for variable permeability taking $E = 10$ kPa and $\kappa_0 = 10^{-13}$ m^2. We also show the maximum vertical displacement at each time. The white dashed line depicts the position of the upper surface at $t = 0$ s. The colormaps are in logarithmic scales to reflect the entire range of pressure and velocity. A deformation scale factor of 5 has been applied to all the figures.

5. Conclusion

The transport and mechanical processes that occur after subcutaneous administration of mAbs are coupled, complex, and remain poorly understood. We have leveraged a three-dimensional poroelastic model to study the tissue deformation and pressure buildup during and after subcutaneous injection. Our model also accounts for permeability changes due to deformation, using a porosity dependent permeability function based on a Kozeny–Carman law. The proposed computational method is based on higher-order globally smooth splines, which have shown to outperform classical C^0-continuous finite elements [14].

To emphasize the importance of poroelasticity effects in subcutaneous injection dynamics, we compare and contrast a rigid porous medium, in which tissue deformation is neglected, a poroelastic medium with constant permeability, and a poroelastic medium with variable porosity and permeability. Our simulations show that tissue deformation plays a critical role in the pressure dynamics, the velocity distribution and, thus, in the way the drug is delivered.

Future efforts will focus on incorporating nonlinear elasticity and the multilayer structure of the tissue in the mechanical model [71]. The transport comportment of the model could be extended, accounting for the viscosity contrast of the drug and the interstitial fluid and incorporating the lymphatic uptake.

Declaration of competing interest

The authors declare that they have no known competing financial interests or personal relationships that could have appeared to influence the work reported in this paper.

Acknowledgments

This work was partially supported by Eli Lilly and Company. The authors thank Kevin Buno for providing the image of the histological section in Fig. 1B.

References

[1] D.S. Dimitrov, Therapeutic proteins, in: Therapeutic Proteins, Springer, 2012, pp. 1–26.

[2] G.B. Jones, D.S. Collins, M.W. Harrison, N.R. Thyagarajapuram, J.M. Wright, Subcutaneous drug delivery: An evolving enterprise, Sci. Transl. Med. 9 (405) (2017) http://dx.doi.org/10.1126/scitranslmed.aaf9166.

[3] E.D. Cock, Y. Pan, S. Tao, P. Baidin, Pcn221 - time savings with transtuzumab subcutaneous (sc) injection verse trastuzumab intravenous (iv) infusion: A time and motion study in 3 russian centers, Value Health 17 (7) (2014) A653, http://dx.doi.org/10.1016/j.jval.2014.08.2380.

[4] X. Pivot, J. Gligorov, V. Müller, G. Curigliano, A. Knoop, S. Verma, V. Jenkins, N. Scotto, S. Osborne, L. Fallowfield, L. Fallowfield, V. Jenkins, J. Kilkerr, C. Langridge, K. Monson, E.H. Jakobsen, M.H. Nielsen, S. Linnet, A. Knoop, X. Pivot, H. Bonnefoi, M. Mousseau, L. Zelek, H. Bourgeois, C.P. Lefeuvre, T. Bachelot, T. Petit, E. Brain, C. Levy, J. Gligorov, D. Augustin, H. Graf, G. Heinrich, H. Kroening, S. Kuemmel, V. Müller, F. Overkamp, T.-W. Park-Simon, M. Schmidt, L. Perlova-Griff, C. Wolf, M. Colleoni, A. Ballestrero, A. Bernardo, A.S. Ribecco, L. Gianni, G. Curigliano, E. Brewczynska, J. Jassem, V. Shirinkin, A. Manikhas, V. Dvornichenko, M. Lichinitser, V. Semiglazov, G. Mukhametshina, I. Bulavina, E.E. Arranz, F.C. Ocon, G.L. Vivanco, J.S. Bofill, I.P. Quintela, A.S. Muoz, Y.F. Pérez, J.C. Espinosa, J.V. Alvarez, R.L. del Prado, L.D.L.C. Merino, J.M.P. Garca, S.E. Frances, P. Edlund, B. Norberg, A.-K. Wennstig, P. Lind, N. Hauser, C. Tausch, C. Camci, F. Arpaci, H. Abali, R. Uslu, S. Tahir, D. Wheatley, S. Chan, P. Barrett-Lee, K. McAdam, R. Simcock, R. Burcombe, R. El-Maraghi, N. Califaretti, S. Spadafora, S. Sehdev, A. Sami, S. Verma, Patients' preferences for subcutaneous trastuzumab versus conventional intravenous infusion for the adjuvant treatment of HER2-positive early breast cancer: final analysis of 488 patients in the international, randomized, two-cohort prefher study, Ann. Oncol. 25 (10) (2014) 1979–1987, http://dx.doi.org/10.1093/annonc/mdu364.

[5] M.F. Haller, Converting intravenous dosing to subcutaneous dosing with recombinant human hyaluronidase, Pharm. Technol. 31 (10) (2007).

[6] L. Bookbinder, A. Hofer, M. Haller, M. Zepeda, G.-A. Keller, J. Lim, T. Edgington, H. Shepard, J. Patton, G. Frost, A recombinant human enzyme for enhanced interstitial transport of therapeutics, J. Control. Release 114 (2) (2006) 230–241.

[7] O. Shpilberg, C. Jackisch, Subcutaneous administration of rituximab (mabthera) and trastuzumab (herceptin) using hyaluronidase, British J. Cancer 109 (6) (2013) 1556–1561.

[8] C. Jackisch, V. Müller, C. Maintz, S. Hell, B. Ataseven, Subcutaneous administration of monoclonal antibodies in oncology, Geburtshilfe Frauenheilkd. 74 (4) (2014) 343.

[9] D.S. Tomar, S. Kumar, S.K. Singh, S. Goswami, L. Li, Molecular basis of high viscosity in concentrated antibody solutions: Strategies for high concentration drug product development, mAbs 8 (2) (2016) 216–228, http://dx.doi.org/10.1080/19420862.2015.1128606, pMID: 26736022.

[10] H. Kim, H. Park, S.J. Lee, Effective method for drug injection into subcutaneous tissue, Sci. Rep. 7 (1) (2017) 1–11.

[11] M. Thomsen, A. Hernandez-Garcia, J. Mathiesen, M. Poulsen, D.N. Srensen, L. Tarnow, R. Feidenhans'l, Model study of the pressure build-up during subcutaneous injection, PLOS ONE 9 (8) (2014) 1–7, http://dx.doi.org/10.1371/journal.pone.0104054.

[12] S. Barry, G. Aldis, G. Mercer, Injection of fluid into a layer of deformable porous medium, Appl. Mech. Rev. 48 (10) (1995) 722–726, http://dx.doi.org/10.1115/1.3005054.

[13] S. Barry, G. Mercer, C. Zoppou, Deformation and fluid flow due to a source in a poro-elastic layer, Appl. Math. Model. 21 (11) (1997) 681–689.

[14] F. Irzal, J.J.C. Remmers, C.V. Verhoosel, R. de Borst, Isogeometric finite element analysis of poroelasticity, Int. J. Numer. Anal. Methods Geomech. 37 (12) (2013) 1891–1907, http://dx.doi.org/10.1002/nag.2195.

[15] S. Morganti, C. Callari, F. Auricchio, A. Reali, Mixed isogeometric collocation methods for the simulation of poromechanics problems in 1d, Meccanica 53 (6) (2018) 1441–1454.

[16] L.T. Baxter, H. Zhu, D.G. Mackensen, R.K. Jain, Physiologically based pharmacokinetic model for specific and nonspecific monoclonal antibodies and fragments in normal tissues and human tumor xenografts in nude mice, Cancer Res. 54 (6) (1994) 1517–1528, arXiv:https://cancerres.aacrjournals.org/content/54/6/1517.full.pdf. URL https://cancerres.aacrjournals.org/content/54/6/1517.

[17] L. Possenti, G. Casagrande, S. Di Gregorio, P. Zunino, M.L. Costantino, Numerical simulations of the microvascular fluid balance with a non-linear model of the lymphatic system, Microvasc. Res. 122 (2019) 101–110, http://dx.doi.org/10.1016/j.mvr.2018.11.003, URL http://www.sciencedirect.com/science/article/pii/S0026286218300384.

[18] A. Coclite, S. Ranaldo, M. de Tullio, P. Decuzzi, G. Pascazio, Kinematic and dynamic forcing strategies for predicting the transport of inertial capsules via a combined lattice Boltzmann – immersed boundary method, Comput. & Fluids 180 (2019) 41–53, http://dx.doi.org/10.1016/j.compfluid.2018.12.014, URL http://www.sciencedirect.com/science/article/pii/S0045793018304304.

[19] K.I. Jerg, R.P. Austermühl, K. Roth, J. Große Sundrup, G. Kanschat, J.W. Hesser, L. Wittmayer, Diffuse domain method for needle insertion simulations, Int. J. Numer. Methods Biomed. Eng. 36 (9) (2020) e3377, http://dx.doi.org/10.1002/cnm.3377, arXiv:https://onlinelibrary.wiley.com/doi/pdf/10.1002/cnm.3377. URL https://onlinelibrary.wiley.com/doi/abs/10.1002/cnm.3377.

[20] M.A. Biot, General theory of threedimensional consolidation, J. Appl. Phys. 12 (2) (1941) 155–164, http://dx.doi.org/10.1063/1.1712886.

[21] M.A. Biot, G. Temple, Theory of finite deformations of porous solids, Indiana Univ. Math. J. 21 (7) (1972) 597–620.

[22] M.A. Swartz, M.E. Fleury, Interstitial flow and its effects in soft tissues, Annu. Rev. Biomed. Eng. 9 (2007) 229–256.

[23] H. Steeb, J. Renner, Mechanics of poro-elastic media: A review with emphasis on foundational state variables, Transp. Porous Media 130 (2) (2019) 437–461.

[24] B.R. Simon, Multiphase poroelastic finite element models for soft tissue structures, Appl. Mech. Rev. 45 (6) (1992).

[25] L.C. Auton, C.W. MacMinn, From arteries to boreholes: transient response of a poroelastic cylinder to fluid injection, Proc. R. Soc. A 474 (2216) (2018) 20180284, http://dx.doi.org/10.1098/rspa.2018.0284.

[26] C.W. MacMinn, E.R. Dufresne, J.S. Wettlaufer, Large deformations of a soft porous material, Phys. Rev. Appl. 5 (2016) 044020, http://dx.doi.org/10.1103/PhysRevApplied.5.044020.

[27] R.K. Jain, R.T. Tong, L.L. Munn, Effect of vascular normalization by antiangiogenic therapy on interstitial hypertension, peritumor edema, and lymphatic metastasis: insights from a mathematical model, Cancer Res. 67 (6) (2007) 2729–2735.

[28] G. Vilanova, M. Burés, I. Colominas, H. Gomez, Computational modelling suggests complex interactions between interstitial flow and tumour angiogenesis, J. R. Soc. Interface 15 (146) (2018) 20180415, http://dx.doi.org/10.1098/rsif.2018.0415.

[29] E.A. Swabb, J. Wei, P.M. Gullino, Diffusion and convection in normal and neoplastic tissues, Cancer Res. 34 (10) (1974) 2814–2822.

[30] J.H. Smith, J.A. Humphrey, Interstitial transport and transvascular fluid exchange during infusion into brain and tumor tissue, Microvasc. Res. 73 (1) (2007) 58–73, http://dx.doi.org/10.1016/j.mvr.2006.07.001.

[31] C.T. McKee, J.A. Last, P. Russell, C.J. Murphy, Indentation versus tensile measurements of young's modulus for soft biological tissues, Tissue Eng. B 17 (3) (2011) 155–164, http://dx.doi.org/10.1089/ten.teb.2010.0520, PMID: 21303220.

[32] M. Geerligs, A literature review of the mechanical behavior of the stratum corneum, the living epidermis and the subcutaneous fat tissue, 2006.

[33] A. González-Suárez, E. Gutierrez-Herrera, E. Berjano, J.N. Jimenez Lozano, W. Franco, Thermal and elastic response of subcutaneous tissue with different fibrous septa architectures to rf heating: Numerical study, Lasers Surg. Med. 47 (2) (2015) 183–195, http://dx.doi.org/10.1002/lsm.22301.

[34] C. Li, G. Guan, R. Reif, Z. Huang, R.K. Wang, Determining elastic properties of skin by measuring surface waves from an impulse mechanical stimulus using phase-sensitive optical coherence tomography, J. R. Soc. Interface 9 (70) (2012) 831–841, http://dx.doi.org/10.1098/rsif.2011.0583.

[35] C. Pailler-Mattei, S. Bec, H. Zahouani, In vivo measurements of the elastic mechanical properties of human skin by indentation tests, Med. Eng. Phys. 30 (5) (2008) 599–606, http://dx.doi.org/10.1016/j.medengphy.2007.06.011.

[36] Y.P. Zheng, A.F.T. Mak, Extraction of effective young's modulus of skin and subcutaneous tissues from manual indentation data, in: Proceedings of the 19th Annual International Conference of the IEEE Engineering in Medicine and Biology Society. 'Magnificent Milestones and Emerging Opportunities in Medical Engineering' (Cat. No.97CH36136), Vol. 5, 1997, pp. 2246–2249, http://dx.doi.org/10.1109/IEMBS.1997.758807.

[37] Y.C. Fung, Biomechanics: Mechanical Properties of Living Tissues, Springer-Verlag, New York, 1981.

[38] E.J. Chen, J. Novakofski, W.K. Jenkins, W.D. O'Brien, Young's modulus measurements of soft tissues with application to elasticity imaging, IEEE Trans. Ultrason. Ferroelectr. Freq. Control 43 (1) (1996) 191–194, http://dx.doi.org/10.1109/58.484478.

[39] B. Simon, O. Zienkiewicz, D. Paul, An analytical solution for the transient response of saturated porous elastic solids, Int. J. Numer. Anal. Methods Geomech. 8 (4) (1984) 381–398.

[40] J.T. Podichetty, P.R. Bhaskar, A. Khalf, S.V. Madihally, Modeling pressure drop using generalized scaffold characteristics in an axial-flow bioreactor for soft tissue regeneration, Ann. Biomed. Eng. 42 (6) (2014) 1319–1330, http://dx.doi.org/10.1007/s10439-014-1009-5.

[41] J.T. Podichetty, S.V. Madihally, Modeling of porous scaffold deformation induced by medium perfusion, J. Biomed. Mater. Res. B 102 (4) (2014) 737–748, http://dx.doi.org/10.1002/jbm.b.33054.

[42] D.V. Doughty, C.Z. Clawson, W. Lambert, J.A. Subramony, Understanding subcutaneous tissue pressure for engineering injection devices for large-volume protein delivery, J. Pharm. Sci. 105 (7) (2016) 2105–2113.

[43] T. Thueer, L. Birkhaeuer, D. Reilly, Development of an advanced injection time model for an autoinjector, Med. Devices (Auckl. N.Z.) 11 (2018) 215–224.

[44] T. Hughes, J. Cottrell, Y. Bazilevs, Isogeometric analysis: Cad, finite elements, nurbs, exact geometry and mesh refinement, Comput. Methods Appl. Mech. Engrg. 194 (39) (2005) 4135–4195, http://dx.doi.org/10.1016/j.cma.2004.10.008.

[45] I. Akkerman, Y. Bazilevs, V. Calo, T. Hughes, S. Hulshoff, The role of continuity in residual-based variational multiscale modeling of turbulence, Comput. Mech. 41 (3) (2008) 371–378.

[46] J.A. Evans, Y. Bazilevs, I. Babuška, T.J. Hughes, N-widths, sup–infs, and optimality ratios for the k-version of the isogeometric finite element method, Comput. Methods Appl. Mech. Engrg. 198 (21–26) (2009) 1726–1741.

[47] H. Gómez, V.M. Calo, Y. Bazilevs, T.J. Hughes, Isogeometric analysis of the cahn–hilliard phase-field model, Comput. Methods Appl. Mech. Engrg. 197 (49) (2008) 4333–4352, http://dx.doi.org/10.1016/j.cma.2008.05.003, URL http://www.sciencedirect.com/science/article/pii/S0045782508001953.

[48] H. Gomez, T.J. Hughes, X. Nogueira, V.M. Calo, Isogeometric analysis of the isothermal navier–stokes–korteweg equations, Comput. Methods Appl. Mech. Engrg. 199 (25) (2010) 1828–1840, http://dx.doi.org/10.1016/j.cma.2010.02.010, URL http://www.sciencedirect.com/science/article/pii/S004578251000068X.

[49] H. Gomez, X. Nogueira, An unconditionally energy-stable method for the phase field crystal equation, Comput. Methods Appl. Mech. Engrg. 249–252 (2012) 52–61, http://dx.doi.org/10.1016/j.cma.2012.03.002, higher Order Finite Element and Isogeometric Methods. URL http://www.sciencedirect.com/science/article/pii/S0045782512000692.

[50] F. Auricchio, L.B. Da Veiga, T.J.R. Hughes, A. Reali, G. Sangalli, Isogeometric collocation methods, Math. Models Methods Appl. Sci. 20 (11) (2010) 2075–2107, http://dx.doi.org/10.1142/S0218202510004878, arXiv:https://doi.org/10.1142/S0218202510004878.

[51] H. Gomez, L.D. Lorenzis, The variational collocation method, Comput. Methods Appl. Mech. Engrg. 309 (2016) 152–181, http://dx.doi.org/10.1016/j.cma.2016.06.003, URL http://www.sciencedirect.com/science/article/pii/S0045782516305035.

[52] T. Elguedj, Y. Bazilevs, V.M. Calo, T.J. Hughes, B and f projection methods for nearly incompressible linear and non-linear elasticity and plasticity using higher-order nurbs elements, Comput. Methods Appl. Mech. Engrg. 197 (33–40) (2008) 2732–2762.

[53] R. Taylor, Isogeometric analysis of nearly incompressible solids, Internat. J. Numer. Methods Engrg. 87 (1–5) (2011) 273–288.

[54] F. Auricchio, L.B. da Veiga, A. Buffa, C. Lovadina, A. Reali, G. Sangalli, A fully "locking-free" isogeometric approach for plane linear elasticity problems: A stream function formulation, Comput. Methods Appl. Mech. Engrg. 197 (1–4) (2007) 160–172.

[55] O. Zienkiewicz, R. Taylor, J. Zhu, Chapter 18 - computer procedures for finite element analysis, in: O. Zienkiewicz, R. Taylor, J. Zhu (Eds.), The Finite Element Method: Its Basis and Fundamentals (Seventh Edition), seventh ed., Butterworth-Heinemann, Oxford, 2013, pp. 641–645, http://dx.doi.org/10.1016/B978-1-85617-633-0.00018-6.

[56] Z. Ge, Y. He, Y. He, A lowest equal-order stabilized mixed finite element method based on multiphysics approach for a poroelasticity model, Appl. Numer. Math. 153 (2020) 1–14.

[57] I. Shovkun, D.N. Espinoza, Propagation of toughness-dominated fluid-driven fractures in reactive porous media, Int. J. Rock Mech. Min. Sci. 118 (2019) 42–51.

[58] J. Wan, L.J. Durlofsky, T.J.R. Hughes, K. Aziz, Stabilized finite element methods for coupled geomechanics - reservoir flow simulations, Soc. Pet. Eng. (2003) http://dx.doi.org/10.2118/79694-MS.

[59] P.A. Vermeer, A. Verruijt, An accuracy condition for consolidation by finite elements, Int. J. Numer. Anal. Methods Geomech. 5 (1) (1981) 1–14, http://dx.doi.org/10.1002/nag.1610050103.

[60] T.J. Hughes, The Finite Element Method: Linear Static and Dynamic Finite Element Analysis, Courier Corporation, 2012.

[61] Y.W. Bekele, E. Fonn, T. Kvamsdal, A.M. Kvarving, S. Nordal, On mixed isogeometric analysis of poroelasticity, 2017, arXiv preprint arXiv:1706.01275.

[62] K.E. Jansen, C.H. Whiting, G.M. Hulbert, A generalized-α method for integrating the filtered navier–stokes equations with a stabilized finite element method, Comput. Methods Appl. Mech. Engrg. 190 (3–4) (2000) 305–319.

[63] J. Chung, G.M. Hulbert, A time integration algorithm for structural dynamics with improved numerical dissipation: The generalized-α method, J. Appl. Mech. 60 (2) (1993) 371–375, http://dx.doi.org/10.1115/1.2900803.

[64] J. Kim, H.A. Tchelepi, R. Juanes, Stability, accuracy, and efficiency of sequential methods for coupled flow and geomechanics, SPE J. 16 (02) (2011) 249–262, http://dx.doi.org/10.2118/119084-PA.

[65] Y. Saad, M.H. Schultz, Gmres: A generalized minimal residual algorithm for solving nonsymmetric linear systems, SIAM J. Sci. Stat. Comput. 7 (3) (1986) 856–869, http://dx.doi.org/10.1137/0907058.

[66] L. Dalcin, N. Collier, P. Vignal, A. Côrtes, V. Calo, Petiga: A framework for high-performance isogeometric analysis, Comput. Methods Appl. Mech. Engrg. 308 (2016) 151–181, http://dx.doi.org/10.1016/j.cma.2016.05.011, URL http://www.sciencedirect.com/science/article/pii/S0045782516303401.

[67] S. Balay, S. Abhyankar, M.F. Adams, J. Brown, P. Brune, K. Buschelman, L. Dalcin, A. Dener, V. Eijkhout, W.D. Gropp, D. Karpeyev, D. Kaushik, M.G. Knepley, D.A. May, L.C. McInnes, R.T. Mills, T. Munson, K. Rupp, P. Sanan, B.F. Smith, S. Zampini, H. Zhang, H. Zhang, PETSc web page, 2019, https://www.mcs.anl.gov/petsc.

[68] A. Gnanaskandan, K. Mahesh, A numerical method to simulate turbulent cavitating flows, Int. J. Multiph. Flow. 70 (2015) 22–34, http://dx.doi.org/10.1016/j.ijmultiphaseflow.2014.11.009, URL http://www.sciencedirect.com/science/article/pii/S0301932214002298.

[69] N. Semenov, S. Kosterin, Results of studying the speed of sound in moving gas-liquid systems., Teploenergetika 11 (6) (1964) 46–51.

[70] R.E. Henry, M.A. Grolmes, H.K. Fauske, Pressure-pulse propagation in two-phase one- ?and two-component mixtures, 1971, http://dx.doi.org/10.2172/4043485.

[71] M. de Lucio, M.F. García, J.D. García, L.E.R. Rodríguez, F. lvarez Marcos, On the importance of tunica intima in the aging aorta: a three-layered in silico model for computing wall stresses in abdominal aortic aneurysms, Comput. Methods Biomech. Biomed. Eng. (2020) http://dx.doi.org/10.1080/10255842.2020.1836167.